HHS Public Access

Author manuscript

Neuroscience. Author manuscript; available in PMC 2019 January 15.

Published in final edited form as:

Neuroscience. 2018 January 15; 369: 40–50. doi:10.1016/j.neuroscience.2017.10.035.

Thermal Stimulation Alters Cervical Spinal Cord Functional Connectivity in Humans

Kenneth A. Weber II[a], **Amy I. Sentis**[a], **Olivia N. Bernadel-Huey**[a], **Yufen Chen**[b], **Xue Wang**[b], **Todd B. Parrish**[b], and **Sean Mackey**[a]

[a]Systems Neuroscience and Pain Lab, Department of Anesthesia, Perioperative and Pain Medicine, Stanford University, Palo Alto, CA, USA, 94304

[b]Department of Radiology, Northwestern University, Chicago, IL, USA, 60611

Abstract

The spinal cord has an active role in the modulation and transmission of the neural signals traveling between the body and the brain. Recent advancements in functional magnetic resonance imaging (fMRI) have made the *in vivo* examination of spinal cord function in humans now possible. This technology has been recently extended to the investigation of resting state functional networks in the spinal cord, leading to the identification of distinct patterns of spinal cord functional connectivity. In this study, we expand on the previous work and further investigate resting state cervical spinal cord functional connectivity in healthy participants (n = 15) using high resolution imaging coupled with both seed-based functional connectivity analyses and graph theory-based metrics. Within spinal cord segment functional connectivity was present between the left and right ventral horns (bilateral motor network), left and right dorsal horns (bilateral sensory network), and the ipsilateral ventral and dorsal horns (unilateral sensory-motor network). Functional connectivity between the spinal cord segments was less apparent with the connectivity centered at the region of interest and spanning < 20 mm along the superior-inferior axis. In a subset of participants (n = 10), the cervical spinal cord functional network was demonstrated to be state-dependent as thermal stimulation of the right ventrolateral forearm resulted in significant disruption of the bilateral sensory network, increased network global efficiency, and decreased network modularity.

Keywords

Humans; Functional MRI; Spinal Cord; Resting State; Upper Extremity; Sensory Function

CORRESPONDING AUTHOR: Kenneth A. Weber II, DC, PhD, Postdoctoral Scholar, Systems Neuroscience and Pain Lab, Department of Anesthesia, Perioperative and Pain Medicine, Stanford University, 1070 Arastradero Road, Suite 200, Palo Alto, California 94304, +1 847-997-6299 (Mobile), +1 650-724-2065 (Work), kenweber@stanford.edu.

INTRODUCTION

The spinal cord is the caudal extension of the brainstem and has an active role in the modulation and transmission of the neural signals traveling between the body and the brain. Disruption of this information flow through injury or disease can cause sensory, motor, and autonomic dysfunction and a plethora of signs and symptoms. Much of our understanding of the neurophysiology and pathophysiology of the spinal cord has been gained through animal research. While animal studies have provided significant information, animal models are limited in their ability to replicate clinical conditions (Berge, 2011), and innovative methods to directly study spinal cord function in humans are necessary to fully understand the neuropathophysiology of the spinal cord in diseased states.

Recent advancements in functional magnetic resonance imaging (fMRI) and the release of sophisticated tools specifically designed for the analysis of spinal cord images have made the quantitative non-invasive assessment of spinal cord function in humans now possible (Nash et al., 2013; Wheeler-Kingshott et al., 2014; Eippert et al., 2016; Weber et al., 2016a, b; De Leener et al., 2017), and a growing body of researchers are working to use this new technology to aid in the diagnosis, prognosis, and treatment of diseases afflicting the spinal cord (Martin et al., 2016). The bulk of spinal cord fMRI studies to date have utilized task-based designs investigating spinal cord activity during sensory, motor, and/or cognitive manipulations. Recently this line of research has been extended to the study of the intrinsic resting state spinal cord functional networks, in which the temporal covariance between signals in regions across the spinal cord are assessed. These studies have discovered novel patterns of functional connectivity within the spinal cord, (Barry et al., 2014; Kong et al., 2014; Barry et al., 2016; Eippert et al., 2017) and evidence in non-human primates that the spinal cord functional connectivity may be disrupted by disease or injury (Chen et al., 2015; Liu et al., 2016a). Whether the spinal cord functional network can be modified during an experimental manipulation in humans remains to be investigated.

Here we build on the previous work and characterize the resting state functional connectivity in healthy participants using high-resolution imaging coupled with seed-based functional connectivity measures and graph theory-based metrics. Then in a subset of participants in which imaging was performed during rest and thermal stimulation, we explore state-dependent changes in the cervical spinal cord functional network.

EXPERIMENTAL PROCEDURES

Study participants

Healthy volunteers were recruited as part of two fMRI studies exploring cervical spinal cord activity. One experiment involved an isometric upper extremity motor task (n = 11), and the second involved thermal stimulation of the right ventrolateral forearm (n = 12) (Weber et al., 2016a, b). In a subset of 16 participants from these two studies (mean age ± 1 standard deviation = 28.3 ± 2.4 years, 6 females), resting state functional images of the cervical spinal cord were also obtained and analyzed in the present study. Prior to participation, the study personnel informed the participants of the study procedures, and each participant provided

written informed consent. All study procedures were approved by Northwestern University's Institutional Review Board.

Image acquisition

Imaging was performed using a 3T Siemens Prisma (Munich, Germany) magnetic resonance (MR) scanner with the participants positioned supine on the scanner bed. The scanner was equipped with a 64-channel head/neck coil, and the head coil elements 5–7 (inferior portion of the head coil) and the anterior and posterior neck coil elements (24 channels) were used to capture the MR signal. During imaging, a SatPad™ cervical collar was used to increase the magnetic field homogeneity across the cervical spine and reduce bulk motion (Maehara et al., 2014). High-resolution resting state functional images of the cervical spinal cord were acquired with a T_2*-weighted gradient-echo echo-planar-imaging sequence using ZOOMit selective field-of-view imaging (6 min 40 s, 160 volumes, TR_{3D} = 2500 ms, TE = 30 ms, flip angle = 80°, slice order = interleaved, acquisition matrix = 128 × 44, field-of-view = 128 × 44 mm^2, in-plane resolution = 1.0 × 1.0 mm^2, slice thickness = 3.0 mm, discarded 2 dummy volumes) (Pfeuffer et al., 2002; Rieseberg et al., 2002). The imaged volume was aligned parallel to the body of the fifth cervical vertebra and spanned from the inferior endplate of the third cervical vertebra to the superior endplate of the first thoracic vertebra with shimming optimized over the spinal canal. For registration of the resting state functional images to template space, a high-resolution T_2-weighted structural image of the entire cervical spine and upper thoracic spine was acquired using a single slab three-dimensional turbo spin echo sequence with a slab selective, variable excitation pulse (SPACE, TR = 1500 ms, TE_{eff} = 115 ms, echo train length = 78, flip angle = 90°/140°, effective resolution = 0.8 × 0.8 × 0.8 mm^3, interpolated resolution = 0.8 × 0.4 × 0.4 mm^3) (Mugler et al., 2000; Lichy et al., 2005).

Image preprocessing

Motion correction—Image preprocessing and statistical analyses were performed using the Oxford Center for fMRI of the Brain's (FMRIB) Software Library (FSL) and the Spinal Cord Toolbox (Jenkinson et al., 2012; De Leener et al., 2017). Motion correction of the resting state functional time series was performed in two phases using FMRIB's Linear Image Registration Tool (cost function = normalized correlation, interpolation = spline) (Jenkinson et al., 2002). To exclude areas of non-rigid motion outside the vertebral column due to the respiratory cycle and swallowing, a manually drawn binary vertebral column mask was used to weight the reference image. For the first phase of motion correction, the images across the time series were realigned to the middle volume using a three-dimensional rigid body realignment. The mean image across the time series was then calculated, and the realignment procedure was repeated using the mean image as the reference volume. For the second phase of motion correction, a two-dimensional rigid realignment was performed independently for each axial slice using the mean image from the first phase of motion correction as the reference volume to correct for slice-independent motion (Cohen-Adad et al., 2009; Weber II et al., 2014). For quality control at each stage of motion correction, the image time series was visually inspected, and the temporal signal-to-noise ratio (TSNR) over the spinal cord was calculated and compared. As motion correction does not correct for all motion-related noise, motion outlier volumes were identified with FSL's motion outlier

detection tool using the intensity-based DVARS (root mean square variance of the temporal derivative of the time courses) metric and the default threshold (box-plot cutoff = 75^{th} percentile + 1.5 × interquartile range (IQR)) (Power et al., 2012).

Spatial normalization—The MNI-Poly-AMU T_2-weighted spinal cord template (resolution = 0.5 × 0.5 × 0.5 mm^3) was used for spatial normalization (Fonov et al., 2014). First, the T_2-weighted structural image of the cervical spine was cropped to only include the C2 to T1 vertebrae. The spinal cord was then segmented from the cropped images, and a vertebral landmarks mask was manually generated (De Leener et al., 2014). The T_2-weighted image was then straightened along the spinal cord using the spinal cord segmentation mask, and the structural to template registration was performed using the vertebral landmarks mask to locate the vertebral levels, an affine transformation along the superior-inferior axis, and a non-rigid symmetric normalization in the axial plane (i.e., structural to template). For coregistration of the functional images to structural space, the spinal cord was first manually segmented from the mean motion-corrected functional image. Then the mean motion-corrected functional image and the template image (warped to structural space) were initially registered using the spinal cord segmentation masks followed by a non-linear registration constrained to the axial plane (i.e., functional to structural). The deformation fields from each step were then concatenated allowing for the forward transformation of the functional images to template space and the reverse transformation of region of interest (ROI) template masks to functional space (e.g., MNI-Poly-AMU white matter probability mask) (Fonov et al., 2014).

Image denoising—Participant motion, the cardiac and respiratory cycles, and cerebrospinal fluid (CSF) pulsations are significant sources of noise for spinal cord fMRI (Giove et al., 2004). To account for the cardiac and respiratory noise, the respiratory signals, cardiac signals, and MRI volume triggers were collected during scanning (sampling rate = 400 Hz, PowerLab 8/30, ADInstruments Inc., Colorado Springs, CO, USA), and slice specific cardiac and respiratory noise regressors were generated using FSL's physiological noise modeling (PNM) tool (Brooks et al., 2008; Kong et al., 2012). This approach is based on the retrospective correction of physiological motion effects model (RETROICOR) described by Glover et al. (2000) where each slice is assigned a cardiac and respiratory phase, and then the respiratory and cardiac signals are modeled using a Fourier series (sine and cosine terms) with the principal frequency and the next three harmonics (Glover et al., 2000). Multiplicative terms were also generated to account for the interactions between the cardiac and respiratory cycles resulting in a total of 32 regressors. Next, a CSF mask was manually drawn using the mean motion-corrected functional image, and a slice-specific CSF noise regressor was generated from the mean CSF signal at each slice. Removal of the white matter signal is a common approach in resting state fMRI analyses (Caballero-Gaudes and Reynolds, 2016). To extract the white matter signal, the MNI-Poly-AMU template white matter probability map was thresholded at 0.5, eroded to ensure no overlap with the spinal cord gray matter, and warped to functional space. Then a slice-specific white matter noise regressor was generated from the mean white matter signal at each slice.

The motion correction parameters (i.e., x, y, and z rotations and translations from the first phase of motion correction) and physiological noise regressors (cardiac, respiratory, CSF, and white matter signals) were then regressed from the functional time series using FMRIB's Improved Linear Model (FILM). The denoised functional time series was then slice-timing corrected, bandpass filtered (0.010 Hz to 0.198 Hz), and warped to the MNI-Poly-AMU spinal cord template. In template space, the spinal cord gray matter was then extracted from the time series using the MNI-Poly-AMU template gray matter probability map (thresholded at 0.5).

Seed-based functional connectivity

Functional connectivity across the entire cervical spinal cord was explored using a seed-based ROI approach. Left-ventral (LV), left-dorsal (LD), right-dorsal (RD), and right-ventral (RV) spinal cord horn ROI masks at eleven locations evenly distributed superiorly and inferiorly across the cervical spinal cord were generated using the MNI-Poly-AMU gray matter probability maps (44 ROI's in total). The ROI's spanned 6 slices (3.0 mm) and were separated by 6 slices (3.0 mm) (Fig. 1). For each participant, the mean denoised time series was extracted from each ROI, Pearson's correlation coefficients were calculated between the ROI's, and correlation matrices were generated. No spatial smoothing was performed before the extraction of the ROI time series to prevent mixing of signals between the dorsal and ventral horns. To assess the strength of functional connectivity between the LV, LD, RD, and RV spinal cord horns, the Fisher transformation of the correlation coefficients was calculated, and the mean ventral-ventral (V-V), dorsal-dorsal (D-D), ventral-dorsal within hemicord (V-D within), and ventral-dorsal between hemicord (V-D between) connectivity strength across the ROI's were calculated for each participant and compared.

To explore the spatial extent of functional connectivity, subject-level statistical connectivity maps from the denoised time series were generated for each ROI using FILM. The design matrix included the mean time-series for each ROI as the explanatory variable and the temporal masks of any motion outlier volumes as covariates of no interest. Prior to the generation of the subject-level functional connectivity maps, a $2 \times 2 \times 6$ mm^3 full width half maximum (FWHM) Gaussian smoothing kernel was applied to the normalized functional time series to improve the signal-to-noise ratio and increase sensitivity. Average group-level statistical connectivity maps for each ROI were then generated using FMRIB's Local Analysis of Mixed Effects (FLAME) stages 1 and 2. Significant connectivity at the group-level was identified using a cluster-level, family-wise error (FWE) corrected threshold of $p < 0.05$ (cluster-defining threshold $Z > 1.64$ ($p < 0.05$)) to correct for multiple comparisons. Functional connectivity ipsilateral and contralateral to each ROI was explored within the plane of each ROI (i.e., within segment functional connectivity) and between adjacent spinal cord levels (i.e., between segment functional connectivity) using small volume correction. The number of connected voxels in the LV, LD, RV, and RD spinal cord horns across the entire spinal cord were calculated to quantify and compare the spatial localization of the functional connectivity.

Graph theory-based metrics

The topological properties of the cervical spinal cord functional network were then explored using graph theory-based metrics. Graph theory-based metrics summarize the properties of complex networks and are having increased application in the study of functional brain networks (Rubinov and Sporns, 2010). The GraphVar Toolbox was used to process and extract the weighted, undirected global clustering coefficient, global efficiency, modularity, and small-worldness graph metrics from each participant using the absolute value of the correlation matrices over a range of link densities (10%, 20%, 30%, 40%, and 50%) (Rubinov and Sporns, 2010; Kruschwitz et al., 2015). The metrics were normalized using the random networks generated by calculating 100 participant specific random networks with 5,000 iterations. The global clustering coefficient is a measure of functional segregation and describes the interconnectedness of neighboring nodes. Global efficiency is a measure of functional integration with increased efficiency equating to an increased ability to integrate information across the network. Modularity is a measure of segregation within the functional network and represents the degree that the network can be subdivided into separate groups. Small-worldness describes the ratio between segregation of function and integration of information across the network and is calculated by dividing the clustering coefficient of a network normalized by the clustering coefficient of a random network (C/C_r) by the characteristic path length of a network normalized by the characteristic path length of a random network (L/L_r) (Rubinov and Sporns, 2010).

State-dependent functional connectivity

In a subset of participants (n = 10, 28.4 ± 2.7 years, 2 females) in which imaging was also performed during both rest and thermal stimulation of the right ventrolateral forearm, state-dependent changes in the cervical spinal cord functional network were explored. For thermal stimulation, ten 7.5 s warm (43 °C) and ten 7.5 s painful (stimulation temperature providing 65/100 pain on a 101-point verbal numerical rating scale, mean temperature ± 1 SE = 46.6 ± 0.5 °C) thermal stimuli were delivered in a randomized order with a varying interstimulus interval during functional imaging of the cervical spinal cord over the same duration as the resting state scans (160 volumes). See Weber et al. (2016a) for a detailed description of the thermal stimulation protocol (Weber et al., 2016a). The same imaging and preprocessing methods described above were used for the collection and analysis of the thermal stimulation images. Functional connectivity and the graph theory metrics were compared between resting and thermal stimulation using repeated measures designs.

Statistical analysis

Non-imaging statistical tests were performed in IBM SPSS Statistics for Windows Version 21.0 (IBM Corp., Armonk, NY) using an $\alpha < 0.05$ as the threshold for statistical significance with Bonferroni correction for multiple comparisons.

RESULTS

Data quality assessment

Visual inspection of the resting state functional time series demonstrated substantial movement artifacts in one participant, resulting in the exclusion of this participant's data. The remaining 15 participants (mean age = 28.1 ± 2.4 years, 6 females) were included in the analyses. Motion correction improved the quality of data collection as indicated by the increase in mean TSNR over the spinal cord. The mean TSNR ± 1 standard error (SE) significantly increased from 11.8 ± 0.4 to 14.0 ± 0.2 (paired t-test, $t_{(14)} = 9.530$, $p < 0.001$) following the first phase of motion correction and further increased to 15.1 ± 0.2 (paired t-test, $t_{(14)} = 20.209$, $p < 0.001$) following the second phase of motion correction. The mean percentage of volumes identified as outliers ± 1 SE was 1.2% ± 0.3%. Spatial normalization of the functional time series was successfully performed for each participant. Following all preprocessing steps (motion correction, temporal filtering, denoising, slice-timing correction, and spatial normalization), the mean TSNR within the spinal cord gray matter was 82.0 ± 1.2. A significant linear decrease in TSNR along the z-axis from the superior (mean 85.4.5 ± 1.9) to inferior (mean 78.0 ± 2.0) spinal cord slices was present (repeated measures ANOVA, $F_{(1,14)} = 8.328$, $p = 0.012$). Despite this, the mean TSNR within the ROI's did not vary appreciably (range = 76.9 – 89.8).

Seed-based functional connectivity

Correlation matrices were generated to visualize the functional connectivity across the ROI's. The correlation matrices demonstrated evidence of within segment functional connectivity while between segment functional connectivity was less apparent (Fig. 2 A–B). Across participants, the strength of the ventral-ventral (V-V), dorsal-dorsal (D-D), and ventral-dorsal within hemicord (V-D within) functional connectivity was significantly greater than zero (one-sample t-tests, df = 14, Table 1). A repeated measures ANOVA demonstrated a significant difference between the strength of the V-V, D-D, V-D within hemicord, and V-D between hemicord functional connectivity ($F_{(3,42)} = 9.575$, $p < 0.001$). Post-hoc testing demonstrated that the strength of the V-V, D-D, and V-D within hemicord functional connectivity was significantly greater than the V-D between hemicord functional connectivity (paired t-tests, df = 14, Table 1). The strength of the V-V, D-D, and V-D within hemicord connectivity did not differ significantly (Fig. 2 C–D and Table 1).

To explore the spatial extent of the functional connectivity, group statistical connectivity maps from the denoised time series were generated using the mean time series from the ROI's. Overall, the spatial pattern of functional connectivity paralleled the findings of the correlation analyses with evidence of V-V, D-D, and V-D within hemicord connectivity. V-D between hemicord functional connectivity was the least frequent (Fig. 3). As in the correlation analysis, between spinal cord segment functional connectivity was also less apparent with the spatial extent of the connectivity limited to a single cluster that was located ipsilateral to the ROI, centered at the corresponding ROI, and spanned a mean superior-inferior distance ± 1 SE of 14.3 mm ± 0.5 mm (Fig. 4). The ROI's closest to the C5, C6, C7, and C8 spinal cord segments were used to summarize the within and between segment functional connectivity.

State-dependent functional connectivity

State-dependent changes in the cervical spinal cord functional network were then explored in a subset of participants (n = 10) during resting and thermal stimulation of the right ventrolateral forearm. Thermal stimulation resulted in a significant decrease in the D-D functional connectivity compared to resting while V-V, V-D within hemicord, and V-D between hemicord functional connectivity did not statistically differ (paired t-tests, df = 9, Fig. 5A and Table 2). The graph theory-based metrics of global clustering coefficient ($F_{(1,9)}$ = 0.034, p = 0.857) and small-worldness ($F_{(1,9)}$ = 1.096, p = 0.323) did not demonstrate state-dependent changes. However, global efficiency was significantly greater during thermal stimulation than resting ($F_{(1,9)}$ = 10.475, p = 0.010) while modularity significantly decreased ($F_{(1,9)}$ = 6.176, p = 0.035) (Fig. 5B). As bulk motion can confound connectivity measures, the relationship between global efficiency and modularity and the absolute and relative motion was further interrogated; both metrics were not correlated with motion. State-dependent changes in the functional connectivity maps were also explored using paired designs in FSL with FILM; however, no significant differences in the spatial pattern of functional connectivity between the conditions were identified.

DISCUSSION

In this study, we characterized the resting state functional network of the human cervical spinal cord using seed-based functional connectivity measures and graph theory-based metrics. The seed-based correlation analyses and spatial connectivity maps provided complementary evidence, supporting the presence of V-V, D-D, and V-D within hemicord functional connectivity. Between segment functional connectivity was less apparent with the connectivity centered at the region of interest and spanning < 20 mm along the superior-inferior axis. In a subset of participants with imaging performed during resting and thermal stimulation of the right ventrolateral forearm, we then demonstrated that the pattern of functional connectivity was state-dependent. Thermal stimulation resulted in a significant decrease in D-D functional connectivity, increased network global efficiency, and decreased network modularity. Taken together, these findings demonstrate the feasibility of using functional connectivity measures to detect state-dependent changes in the cervical spinal cord functional network.

The identification of V-V and D-D functional connectivity in the present study corroborates the findings of Barry et al. (2014), who first identified V-V and D-D functional connectivity at 7T in humans (Barry et al., 2014). Based on the distinct functional roles of the ventral (i.e., motor) and dorsal (i.e., sensory) horns of the spinal cord, Barry et al. described the V-V and D-D functional connectivity as bilateral motor and sensory spinal cord networks, respectively, and hypothesized that these networks may be mediated by crossed spinal circuits, such as the crossed-extensor reflex, central pattern generators, and propriospinal connections, which modulate motor and sensory processes between hemicords. Since the original report, the motor and sensory networks have been shown to have moderate intra-subject reliability and were recently identified at 3T (Barry et al., 2016; Eippert et al., 2017).

In addition to corroborating previous findings, here we demonstrated that unilateral thermal stimulation altered the D-D functional connectivity. Cutaneous thermal and thermal-pain

sensations are conveyed primarily by Aδ- and C-fiber thermoreceptors and temperature-sensitive nociceptors, and their axons project mainly to neurons in the ipsilateral dorsal horn of the spinal cord, which is the first central site of thermal and nociceptive processing (Willis and Westlund, 1997; Green, 2004). The unilateral influx of sensory input to the right dorsal horn from the right-sided thermal stimulation may have decreased the synchrony in signals between the left and right dorsal horns, reducing the temporal covariance between these regions and disrupting the bilateral sensory network.

Another novel finding in the present study is the identification of V-D within hemicord functional connectivity. In addition to between hemicord circuits, within hemicord spinal circuits between the ipsilateral ventral and dorsal horns, such as the monosynaptic stretch reflex and nociceptive withdrawal reflex, have also been identified (Pierrot-Deseilligny and Burke, 2012). The existence of these circuits can provide a theoretical ground for the V-D within hemicord functional connectivity identified in the present study. However, the exact neurophysiological mechanisms underlying functional connectivity in the spinal cord remain to be elucidated. The identified functional spinal cord networks (bilateral motor, bilateral sensory, and unilateral sensory-motor networks) likely arise from a combination of afferent input, interneuronal processing, and descending neuromodulation. The ability to detect V-D within hemicord functional connectivity in the present study may be due to differences in the imaging parameters, spatial normalization, or denoising procedures. As spinal cord fMRI is a new field, much remains to be optimized in the space of image acquisition and analysis. Collaborative projects across research sites are currently underway to improve and standardize the methods in the field (Wheeler-Kingshott et al., 2014; Martin et al., 2016; Cohen-Adad, 2017; Prados et al., 2017).

Graph theory-based approaches are commonly used to explore the organization of the functional networks in the brain (for review see (Fornito et al., 2013)), and graph theory-based metrics have been shown to be sensitive to different brain states (e.g., resting versus task) and diseases affecting the central nervous system (Bassett et al., 2006; Mansour et al., 2016). Functional brain networks are often characterized as having small-world properties with high local clustering and short path lengths between nodes due to a few long-range connections. The small world organization of brain networks is theorized to have evolved in order to reduce costs and maintain segregation of function while permitting integration of information across brain regions (Bassett and Bullmore, 2006). Recently, Liu et al. (2016b) applied graph theory-based approaches to assess the network properties of the cervical spinal cord at rest and reported that the spinal cord functional network may have small-world properties (Liu et al., 2016b).

The present study expanded on the work by Liu et al. (2016b) and investigated state-dependent changes in the topological properties of the cervical spinal cord functional network using several graph-based metrics (Liu et al., 2016b). While we also identified small-world properties of the cervical spinal cord network (small-worldness > 1), neither small-worldness nor global clustering coefficient significantly differed between resting and thermal stimulation. However, the graph theory-based metrics of global efficiency and modularity appear to be sensitive to the changes in the spinal cord functional network during unilateral thermal stimulation. The increase in global efficiency suggests that long-distance

connections were increased during thermal stimulation resulting in a reduced characteristic path length of the network. The axons of afferent fibers are known to ascend several spinal cord segments before entering the gray matter of the dorsal horn (Light and Perl, 1979; Coggeshall et al., 1981; Sugiura et al., 1986). The right-sided afferent input from right-sided thermal stimulation may have increased synchrony between the right dorsal horns across the spinal cord segments leading to more long-distance connections and increased global efficiency. Modularity measures the degree to which a network may be subdivided into distinct and separate groups (Rubinov and Sporns, 2010). The reduced modularity during thermal stimulation could also be explained by an increase in synchrony between the right dorsal horns during thermal stimulation, which would reduce the presence of individual groups. The decreased D-D functional connectivity during thermal stimulation may have further reduced the modularity by disrupting the within segment functional network groups. While the within-subject design of the present study provided sufficient power to detect these global changes in the network topology, a larger sample size is necessary to provide a more detailed and comprehensive understanding of how the spinal cord functional network varies in different states. Overall, the application of graph theory metrics to spinal cord fMRI may be helpful in quantitatively summarizing changes in complex spinal cord network properties, which may not be apparent when assessing statistical connectivity maps across several ROI's.

We expected to find evidence of between segment functional connectivity as we hypothesized there to be some exchange of information between spinal cord segments. However, strikingly, we did not find strong evidence of between segment functional connectivity at rest with either the correlation analyses or the spatial connectivity maps. Slice-timing did not seem to attribute to the lack of between segment functional connectivity as the same pattern of connectivity was present with or without slice-timing correction. Based on our findings, the spinal cord functional network appears to have more of a regular, lattice like structure at rest with greater information processing occurring locally within a spinal cord segment than across the superior-inferior axis (Bassett and Bullmore, 2006). We hypothesize that tasks which engage multiple spinal cord segments (i.e., a bilateral upper extremity motor task) will demonstrate increased between segment functional connectivity.

Finally, bulk motion is known to confound functional connectivity measures in the brain (Power et al., 2012). In the present study, we took care to mitigate the effect of motion. The decreased D-D functional connectivity during thermal stimulation was not likely due to motion. Because of the small cross-sectional area of the spinal cord ($< 10\ mm^2$), motion would be expected to modulate functional connectivity measures across the entire spinal cord and not be localized to the dorsal gray matter (Kato et al., 2012). Therefore, the specificity of the connectivity changes to the bilateral sensory network reduces the concerns of motion influencing this finding. The changes in global efficiency and modularity were also not likely due to motion. We thoroughly investigated the association between these graph theory-based metrics and motion and found no significant relationships. Therefore, motion likely had no appreciable influence on the findings.

CONCLUSIONS

Spinal cord fMRI is the only technique currently available to non-invasively study spinal cord processing in humans with high-spatial resolution. Here we confirmed the presence of the bilateral motor (V-V functional connectivity) and sensory (D-D functional connectivity) spinal cord networks, and we identified a unilateral sensory-motor (V-D within hemicord functional connectivity) network. The pattern of functional connectivity and the topological properties of the spinal cord functional network appear to be state-dependent as thermal stimulation disrupted the bilateral sensory connectivity, increased network global efficiency, and decreased network modularity. While this study only investigated heathy participants, the combination of spinal cord fMRI and network based functional connectivity measures may help shape our understanding of the neuropathophysiology of diseases that affect sensory and motor processing in the spinal cord (e.g., chronic pain and spinal cord injury), and the application of these techniques should be explored in clinical populations.

Acknowledgments

Research reported in this publication was supported by the National Institute on Drug Abuse [grant number T32DA035165] and the National Center for Complementary and Integrative Health [grant number F32AT007800]. The content is solely the responsibility of the authors and does not necessarily represent the official views of the National Institutes of Health.

ABBREVIATIONS

MR	magnetic resonance
MRI	magnetic resonance imaging
fMRI	functional magnetic resonance imaging
SPACE	sampling perfection with application optimized contrast using different flip angle evolutions
FMRIB	Oxford Center for Functional MRI of the Brain
FSL	FMRIB’s Software Library
FILM	FMRIB’s Improved Linear Model
ROI	region of interest
FWE	family-wise error
V-V	ventral-ventral
V-D	ventral-dorsal
D-D	dorsal-dorsal
LV	left-ventral
LD	left-dorsal

RD	right-dorsal
RV	right-ventral

References

Barry RL, Rogers BP, Conrad BN, Smith SA, Gore JC. Reproducibility of resting state spinal cord networks in healthy volunteers at 7 Tesla. Neuroimage. 2016; 133:31–40. [PubMed: 26924285]

Barry RL, Smith SA, Dula AN, Gore JC. Resting state functional connectivity in the human spinal cord. eLife. 2014; 3:e02812. [PubMed: 25097248]

Bassett DS, Bullmore E. Small-world brain networks. Neuroscientist. 2006; 12(6):512–523. [PubMed: 17079517]

Bassett DS, Meyer-Lindenberg A, Achard S, Duke T, Bullmore E. Adaptive reconfiguration of fractal small-world human brain functional networks. Proc Natl Acad Sci USA. 2006; 103(51):19518–19523. [PubMed: 17159150]

Berge OG. Predictive validity of behavioural animal models for chronic pain. Br J Pharmacol. 2011; 164(4):1195–1206. [PubMed: 21371010]

Brooks JC, Beckmann CF, Miller KL, Wise RG, Porro CA, Tracey I, Jenkinson M. Physiological noise modelling for spinal functional magnetic resonance imaging studies. Neuroimage. 2008; 39(2):680–692. [PubMed: 17950627]

Caballero-Gaudes C, Reynolds RC. Methods for cleaning the BOLD fMRI signal. Neuroimage. 2016

Chen LM, Mishra A, Yang PF, Wang F, Gore JC. Injury alters intrinsic functional connectivity within the primate spinal cord. Proc Natl Acad Sci USA. 2015; 112(19):5991–5996. [PubMed: 25902510]

Coggeshall RE, Chung K, Chung JM, Langford LA. Primary afferent axons in the tract of Lissauer in the monkey. J Comp Neurol. 1981; 196(3):431–442. [PubMed: 7217365]

Cohen-Adad J. Functional Magnetic Resonance Imaging of the Spinal Cord: Current Status and Future Developments. Semin Ultrasound CT MR. 2017; 38(2):176–186. [PubMed: 28347420]

Cohen-Adad, J., Rossignol, S., Hoge, RD. Slice-by-slice motion correction in spinal cord fMRI: SliceCorr. Proceedings of the 17th Annual Meeting of the International Society for Magnetic Resonance in Medicine; Honolulu, USA. 2009.

De Leener B, Kadoury S, Cohen-Adad J. Robust, accurate and fast automatic segmentation of the spinal cord. Neuroimage. 2014; 98:528–536. [PubMed: 24780696]

De Leener B, Levy S, Dupont SM, Fonov VS, Stikov N, Louis Collins D, Callot V, Cohen-Adad J. SCT: Spinal Cord Toolbox, an open-source software for processing spinal cord MRI data. Neuroimage. 2017; 145(Pt A):24–43. [PubMed: 27720818]

Eippert F, Kong Y, Jenkinson M, Tracey I, Brooks JC. Denoising spinal cord fMRI data: Approaches to acquisition and analysis. Neuroimage. 2016; 154:255–266. [PubMed: 27693613]

Eippert F, Kong Y, Winkler AM, Andersson JL, Finsterbusch J, Buchel C, Brooks JC, Tracey I. Investigating resting-state functional connectivity in the cervical spinal cord at 3T. Neuroimage. 2017; 147:589–601. [PubMed: 28027960]

Fonov VS, Le Troter A, Taso M, De Leener B, Leveque G, Benhamou M, Sdika M, Benali H, Pradat PF, Collins DL, Callot V, Cohen-Adad J. Framework for integrated MRI average of the spinal cord white and gray matter: the MNI-Poly-AMU template. Neuroimage. 2014; 102(Pt 2):817–827. [PubMed: 25204864]

Fornito A, Zalesky A, Breakspear M. Graph analysis of the human connectome: promise, progress, and pitfalls. Neuroimage. 2013; 80:426–444. [PubMed: 23643999]

Giove F, Garreffa G, Giulietti G, Mangia S, Colonnese C, Maraviglia B. Issues about the fMRI of the human spinal cord. Magn Reson Imaging. 2004; 22(10):1505–1516. [PubMed: 15707800]

Glover GH, Li TQ, Ress D. Image-based method for retrospective correction of physiological motion effects in fMRI: RETROICOR. Magn Reson Med. 2000; 44(1):162–167. [PubMed: 10893535]

Green BG. Temperature perception and nociception. J Neurobiol. 2004; 61(1):13–29. [PubMed: 15362150]

Jenkinson M, Bannister P, Brady M, Smith S. Improved optimization for the robust and accurate linear registration and motion correction of brain images. Neuroimage. 2002; 17(2):825–841. [PubMed: 12377157]

Jenkinson M, Beckmann CF, Behrens TE, Woolrich MW, Smith SM. FSL. Neuroimage. 2012; 62(2): 782–790. [PubMed: 21979382]

Kato F, Yukawa Y, Suda K, Yamagata M, Ueta T. Normal morphology, age-related changes and abnormal findings of the cervical spine. Part II: Magnetic resonance imaging of over 1,200 asymptomatic subjects. Eur Spine J. 2012; 21(8):1499–1507. [PubMed: 22302162]

Kong Y, Eippert F, Beckmann CF, Andersson J, Finsterbusch J, Buchel C, Tracey I, Brooks JC. Intrinsically organized resting state networks in the human spinal cord. Proc Natl Acad Sci USA. 2014; 111(50):18067–18072. [PubMed: 25472845]

Kong Y, Jenkinson M, Andersson J, Tracey I, Brooks JC. Assessment of physiological noise modelling methods for functional imaging of the spinal cord. Neuroimage. 2012; 60(2):1538–1549. [PubMed: 22178812]

Kruschwitz JD, List D, Waller L, Rubinov M, Walter H. GraphVar: a user-friendly toolbox for comprehensive graph analyses of functional brain connectivity. J Neurosci Methods. 2015; 245:107–115. [PubMed: 25725332]

Lichy MP, Wietek BM, Mugler JP 3rd, Horger W, Menzel MI, Anastasiadis A, Siegmann K, Niemeyer T, Konigsrainer A, Kiefer B, Schick F, Claussen CD, Schlemmer HP. Magnetic resonance imaging of the body trunk using a single-slab, 3-dimensional, T2-weighted turbo-spin-echo sequence with high sampling efficiency (SPACE) for high spatial resolution imaging: initial clinical experiences. Invest Radiol. 2005; 40(12):754–760. [PubMed: 16304477]

Light AR, Perl ER. Spinal termination of functionally identified primary afferent neurons with slowly conducting myelinated fibers. J Comp Neurol. 1979; 186(2):133–150. [PubMed: 109477]

Liu X, Qian W, Jin R, Li X, Luk KD, Wu EX, Hu Y. Amplitude of Low Frequency Fluctuation (ALFF) in the Cervical Spinal Cord with Stenosis: A Resting State fMRI Study. PLoS One. 2016a; 11(12):e0167279. [PubMed: 27907060]

Liu X, Zhou F, Li X, Qian W, Cui J, Zhou IY, Luk KD, Wu EX, Hu Y. Organization of the intrinsic functional network in the cervical spinal cord: A resting state functional MRI study. Neuroscience. 2016b; 336:30–38. [PubMed: 27590264]

Maehara M, Ikeda K, Kurokawa H, Ohmura N, Ikeda S, Hirokawa Y, Maehara S, Utsunomiya K, Tanigawa N, Sawada S. Diffusion-weighted echo-planar imaging of the head and neck using 3-T MRI: Investigation into the usefulness of liquid perfluorocarbon pads and choice of optimal fat suppression method. Magn Reson Imaging. 2014; 32(5):440–445. [PubMed: 24582547]

Mansour A, Baria AT, Tetreault P, Vachon-Presseau E, Chang PC, Huang L, Apkarian AV, Baliki MN. Global disruption of degree rank order: a hallmark of chronic pain. Sci Rep. 2016; 6:34853. [PubMed: 27725689]

Martin AR, Aleksanderek I, Cohen-Adad J, Tarmohamed Z, Tetreault L, Smith N, Cadotte DW, Crawley A, Ginsberg H, Mikulis DJ, Fehlings MG. Translating state-of-the-art spinal cord MRI techniques to clinical use: A systematic review of clinical studies utilizing DTI, MT, MWF, MRS, and fMRI. Neuroimage Clin. 2016; 10:192–238. [PubMed: 26862478]

Mugler JP 3rd, Bao S, Mulkern RV, Guttmann CR, Robertson RL, Jolesz FA, Brookeman JR. Optimized single-slab three-dimensional spin-echo MR imaging of the brain. Radiology. 2000; 216(3):891–899. [PubMed: 10966728]

Nash P, Wiley K, Brown J, Shinaman R, Ludlow D, Sawyer AM, Glover G, Mackey S. Functional magnetic resonance imaging identifies somatotopic organization of nociception in the human spinal cord. Pain. 2013; 154(6):776–781. [PubMed: 23618495]

Pfeuffer J, van de Moortele PF, Yacoub E, Shmuel A, Adriany G, Andersen P, Merkle H, Garwood M, Ugurbil K, Hu X. Zoomed functional imaging in the human brain at 7 Tesla with simultaneous high spatial and high temporal resolution. Neuroimage. 2002; 17(1):272–286. [PubMed: 12482083]

Pierrot-Deseilligny, E., Burke, DC. The Circuitry of the Human Spinal Cord: Spinal and Corticospinal Mechanisms of Movement. Vol. 1. Cambridge: Cambridge University Press; 2012.

Power JD, Barnes KA, Snyder AZ, Schlaggar BL, Petersen SE. Spurious but systematic correlations in functional connectivity MRI networks arise from subject motion. Neuroimage. 2012; 59(3):2142–2154. [PubMed: 22019881]

Prados F, Ashburner J, Blaiotta C, Brosch T, Carballido-Gamio J, Cardoso MJ, Conrad BN, Datta E, David G, Leener B, Dupont SM, Freund P, Wheeler-Kingshott C, Grussu F, Henry R, Landman BA, Ljungberg E, Lyttle B, Ourselin S, Papinutto N, Saporito S, Schlaeger R, Smith SA, Summers P, Tam R, Yiannakas MC, Zhu A, Cohen-Adad J. Spinal cord grey matter segmentation challenge. Neuroimage. 2017; 152:312–329. [PubMed: 28286318]

Rieseberg S, Frahm J, Finsterbusch J. Two-dimensional spatially-selective RF excitation pulses in echo-planar imaging. Magn Reson Med. 2002; 47(6):1186–1193. [PubMed: 12111965]

Rubinov M, Sporns O. Complex network measures of brain connectivity: uses and interpretations. Neuroimage. 2010; 52(3):1059–1069. [PubMed: 19819337]

Sugiura Y, Lee CL, Perl ER. Central projections of identified, unmyelinated (C) afferent fibers innervating mammalian skin. Science. 1986; 234(4774):358–361. [PubMed: 3764416]

Weber, KA., II, Chen, Y., Wang, X., Parrish, TB. Choice of Motion Correction Method Affects Spinal Cord fMRI Results. 20th Annual Meeting of the Organization for Human Brain Mapping; Hamburg, Germany. 2014.

Weber KA 2nd, Chen Y, Wang X, Kahnt T, Parrish TB. Functional magnetic resonance imaging of the cervical spinal cord during thermal stimulation across consecutive runs. Neuroimage. 2016a; 143:267–279. [PubMed: 27616641]

Weber KA 2nd, Chen Y, Wang X, Kahnt T, Parrish TB. Lateralization of cervical spinal cord activity during an isometric upper extremity motor task with functional magnetic resonance imaging. Neuroimage. 2016b; 125:233–243. [PubMed: 26488256]

Wheeler-Kingshott CA, Stroman PW, Schwab JM, Bacon M, Bosma R, Brooks J, Cadotte DW, Carlstedt T, Ciccarelli O, Cohen-Adad J, Curt A, Evangelou N, Fehlings MG, Filippi M, Kelley BJ, Kollias S, Mackay A, Porro CA, Smith S, Strittmatter SM, Summers P, Thompson AJ, Tracey I. The current state-of-the-art of spinal cord imaging: applications. Neuroimage. 2014; 84:1082–1093. [PubMed: 23859923]

Willis WD, Westlund KN. Neuroanatomy of the pain system and of the pathways that modulate pain. J Clin Neurophysiol. 1997; 14(1):2–31. [PubMed: 9013357]

HIGHLIGHTS

- Resting state functional connectivity was explored in the cervical spinal cord of healthy participants
- High resolution imaging was coupled with seed-based functional connectivity analyses and graph theory-based metrics
- We corroborate previous findings of bilateral motor and sensory spinal cord functional networks
- We provide evidence for the presence of a unilateral sensory-motor spinal cord functional network
- Thermal stimulation altered the pattern of functional connectivity and the topological properties of the functional network

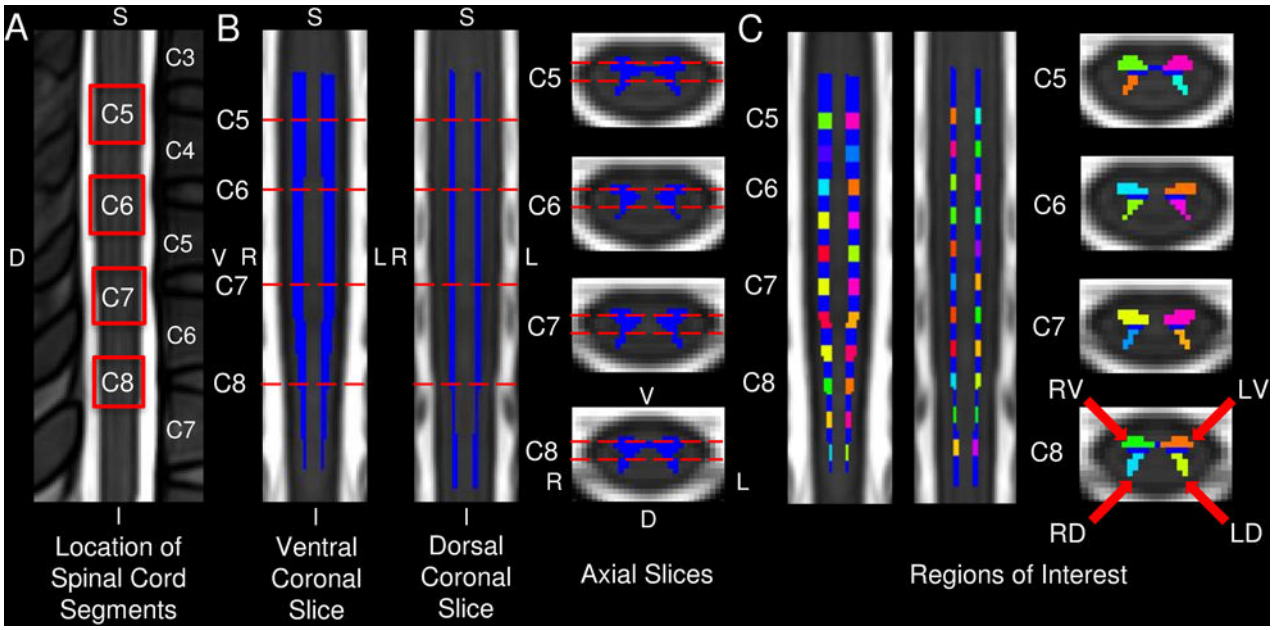

Fig. 1.

The location of the cervical spinal cord segments and 44 region of interest (ROI) masks on the MNI-Poly-AMU T_2-weighted spinal cord template are shown. A) The resting state functional imaging spanned the cervical spinal cord segments C5 through C8, which are outlined in red. The locations of the spinal cord segments were identified using the spinal cord segment probability maps included in the Spinal Cord Toolbox. B) The location of the coronal and axial slices (dashed red lines) used in the corresponding figures are shown with the spinal cord gray matter in blue. C) The 44 ROI masks used in the seed-based functional connectivity analyses are shown and included the left-ventral (LV), left-dorsal (LD), right-dorsal (RD), and right-ventral (RV) spinal cord horns at eleven locations evenly distributed superiorly and inferiorly across the cervical spinal cord. S = superior, I = inferior, V = ventral, D = dorsal, L = left, R = right.

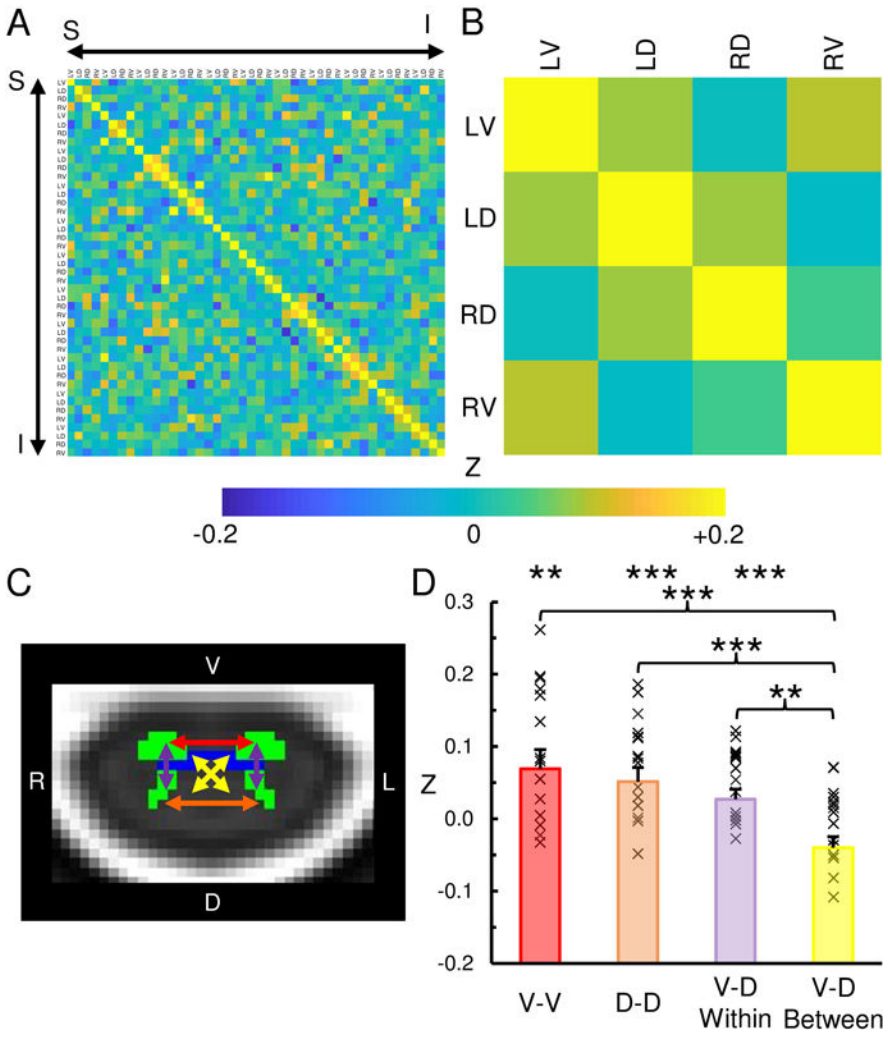

Fig. 2. Cervical spinal cord functional connectivity

Correlation matrices showing the strength of functional connectivity (Fisher Z transformation) between the left-ventral (LV), left-dorsal (LD), right-dorsal (RD), and right-ventral (RV) horns across all regions-of-interest (A) and averaged across the spinal cord levels (B). C) Legend showing ventral-ventral (V-V, red), dorsal-dorsal (D-D, orange), ventral-dorsal within hemicord (V-D within, purple), and ventral-dorsal between hemicord (V-D between, yellow) functional connectivity. D) The strength of the V-D, D-D, and V-D within hemicord functional connectivity was significantly greater than zero and greater than the V-D between hemicord functional connectivity. See Table 1 for the mean correlation strengths and the results of the statistical comparisons. × = correlation value for each participant. Error bars = ± 1 standard error (SE). ** $p < 0.01$, *** $p < 0.001$.

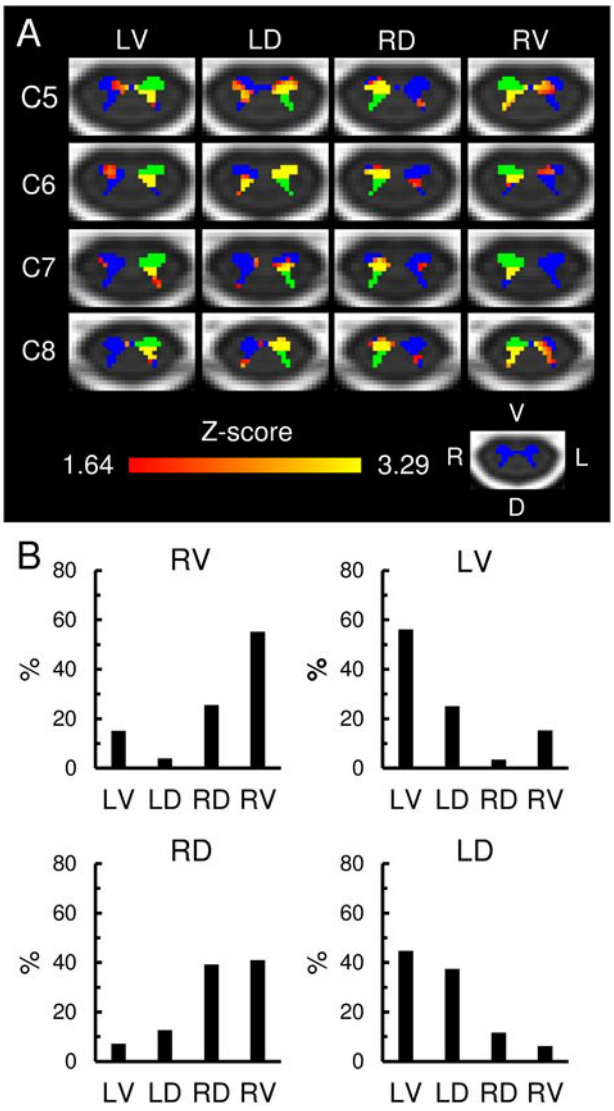

Fig. 3. Within segment functional connectivity

A) Axial slices of the group statistical connectivity maps showing the within segment functional connectivity (Red-Yellow) for the left-ventral (LV), left-dorsal (LD), right-dorsal (RD), and right-ventral (RV) spinal cord horns (shown in green). The within segment functional connectivity is summarized using the regions-of-interest (ROI) closest to the C5, C6, C7, and C8 spinal cord segments. The images show the combined results of the analyses in the ipsilateral and contralateral hemicords. Small volume correction was applied within the plane of each ROI and the corresponding hemicord. The statistical images were thresholded at a cluster-defining threshold of $Z > 1.64$ ($p < 0.05$) followed by a family-wise error (FWE) cluster-level corrected threshold of $p < 0.05$ to correct for multiple comparisons. See Fig. 1 for the location of the slices on the MNI-Poly-AMU spinal cord template. The spinal cord gray matter is shown in blue. B) Bar graphs showing the location of the within segment functional connectivity for the LV, LD, RD, and RV spinal cord horns averaged across all spinal cord levels. L = left, R = right, V = ventral, D = dorsal.

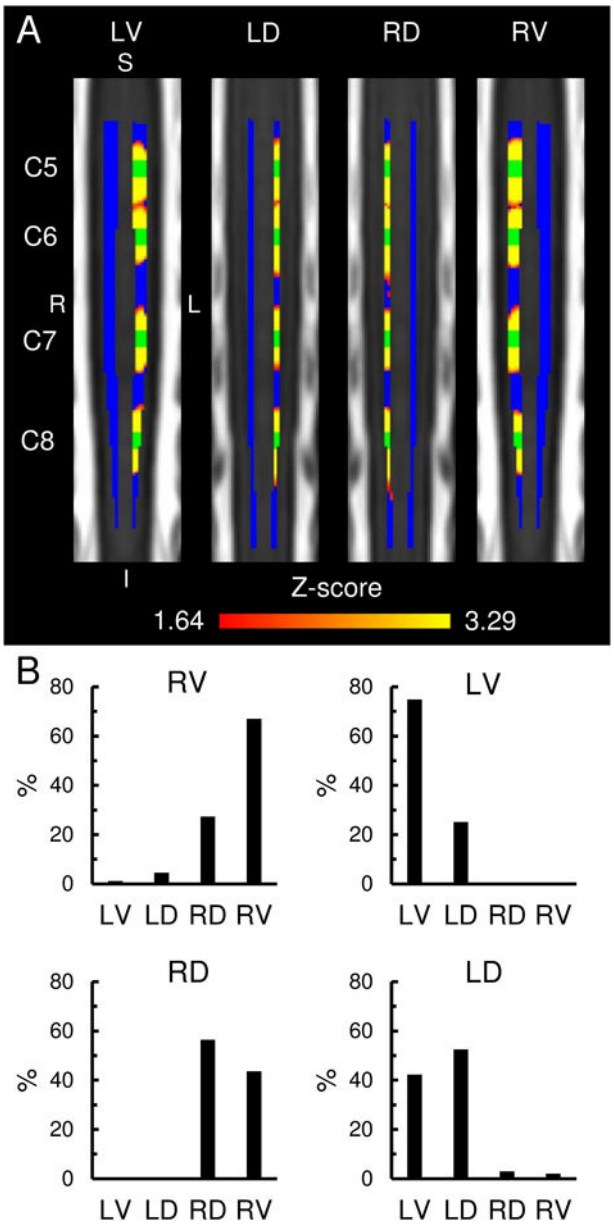

Fig. 4. Between segment functional connectivity

A) Coronal slices of the group statistical connectivity maps showing the functional connectivity between adjacent spinal cord levels (Red-Yellow) for the left-ventral (LV), left-dorsal (LD), right-dorsal (RD), and right-ventral (RV) spinal cord horns using the regions-of-interest (ROI) closest to the C5, C6, C7, and C8 spinal cord segments (shown in green). The spatial extent of the functional connectivity for each ROI was limited primarily to a single cluster that was located ipsilateral to the ROI, centered at the corresponding ROI, and spanned a superior-inferior distance < 20 mm. Each image is an aggregate statistical image of four separate analyses and summarizes the spatial extent of the between segment functional connectivity for the corresponding ROI at the C5, C6, C7, and C8 spinal cord segments. The statistical images were thresholded at a cluster-defining threshold of $Z > 1.64$ ($p < 0.05$) followed by a family-wise error (FWE) cluster-level corrected threshold of $p <$

0.05 to correct for multiple comparisons. See Fig. 1 for the location of the slices on the MNI-Poly-AMU spinal cord template. The spinal cord gray matter is shown in blue. B) Bar graphs showing the location of the between segment functional connectivity for the LV, LD, RD, and RV spinal cord horns averaged across all spinal cord levels. S = superior, I = inferior, L = left, R = right.

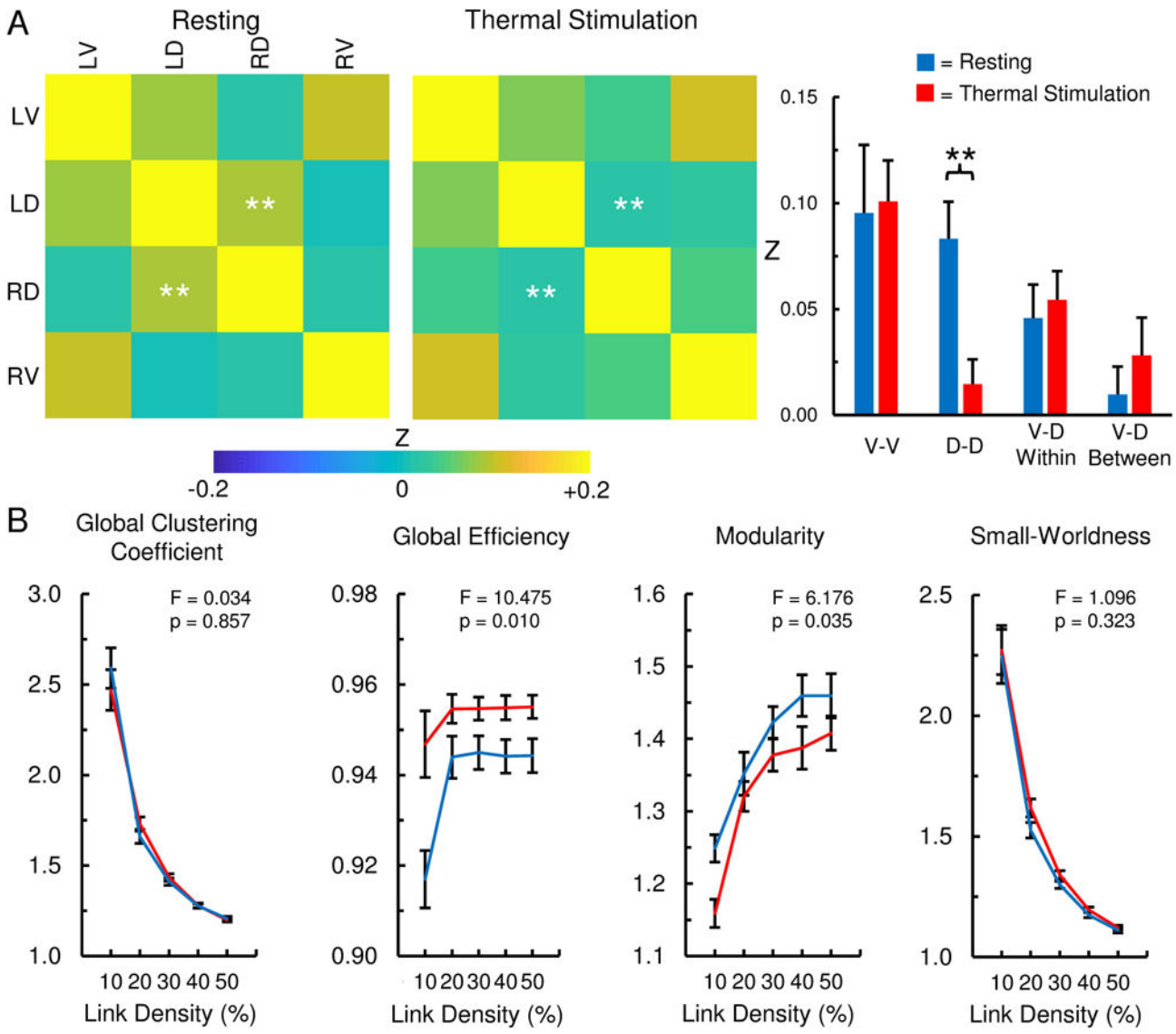

Fig. 5. State-dependent changes in the cervical spinal cord functional network

In a subset of participants (n = 10) with imaging performed at rest and during thermal stimulation of the right ventrolateral forearm, changes in the spinal cord functional network were explored. A) The strength of the dorsal-dorsal (D-D) functional connectivity significantly decreased during thermal stimulation compared to resting. Ventral-ventral (V-V), ventral-dorsal within hemicord (V-D within), and ventral-dorsal between hemicord (V-D between) functional connectivity did not statistically differ between the conditions. See Table 2 for the mean difference in correlation strengths and the results of the statistical comparisons. B) Topological changes in the properties of the functional network were also identified. Global efficiency was significantly greater during thermal stimulation while modularity was significantly decreased. The global clustering coefficient and small-worldness did not statistically differ between the conditions. LV = left ventral, LD = left

dorsal, RD = right dorsal, RV = right ventral. Error bars = ± 1 standard error (SE). **p < 0.01.

Table 1

Within Spinal Cord Segment Functional Connectivity

Mean > 0	**Mean Z ± 1 SE**	**t-value**	**p-value**
V-V	**0.092 ± 0.024**	**3.875**	**0.002**
D-D	**0.076 ± 0.018**	**4.338**	**< 0.001**
V-D Within	**0.055 ± 0.013**	**4.363**	**< 0.001**
V-D Between	−0.006 ± 0.014	-0.421	0.680
Paired Comparisons	**Mean Δ Z ± 1 SE**	**t-value**	**p-value**
V-V > V-D Between	**0.098 ± 0.023**	**4.198**	**< 0.001**
D-D > V-D Between	**0.082 ± 0.016**	**5.184**	**< 0.001**
V-D Within > V-D Between	**0.060 ± 0.018**	**3.422**	**0.004**
V-V > D-D	0.016 ± 0.020	0.786	0.445
V-V > V-D Within	0.038 ± 0.020	1.885	0.080
D-D > V-D Within	0.022 ± 0.020	1.107	0.287

Ventral-ventral (V-V), dorsal-dorsal (D-D), ventral-dorsal within hemicord (V-D within), and ventral-dorsal between hemicord (V-D between) functional connectivity (Fisher's Z transformation) are shown. The strength of the V-V, D-D, and V-D within hemicord functional connectivity was significantly greater than zero and greater than the V-D between hemicord functional connectivity. SE = standard error. Bold font = $p < 0.05$.

Table 2

Change in Connectivity Strength Resting and Thermal Stimulation

Thermal Stimulation - Resting	Mean Δ Z ± 1 SE	t-value	p-value
V-V	0.005 ± 0.030	0.181	0.860
D-D	**−0.069 ± 0.021**	**−3.339**	**0.009**
V-D Within	0.009 ± 0.017	0.514	0.619
V-D Between	0.018 ± 0.015	1.191	0.264

The mean change in functional connectivity strength between resting and thermal stimulation are shown. Thermal stimulation of the right ventral forearm resulted in a significant decrease in dorsal-dorsal (D-D) functional connectivity. Ventral-ventral (V-V), ventral-dorsal within hemicord (V-D within), and ventral-dorsal between hemicord (V-D between) functional connectivity did not statistically differ between resting and thermal stimulation. SE = standard error. Bold font = $p < 0.05$.